High-throughput, In situ Imaging of Multi-layer Powder-blown Directed Energy Deposition with Angled Nozzle

Samantha Webster[1, b)], Marco Giovannini[1], Yi Shi[1], Nicolas Martinez-Prieto[1], Kamel Fezzaa[2], Tao Sun[3], Kornel Ehmann[1], and Jian Cao[1, a)]

[1]*Northwestern University, 2145 Sheridan Rd, Evanston, IL, 60208 USA*
[2]*X-ray Science Division, Argonne National Laboratory, 9700 S Cass Ave., Lemont, IL, 60439 USA*
[3]*University of Virginia, 1827 University Avenue, Charlottesville, VA 22904 USA*

[a)] *Author to whom correspondence should be addressed: jcao@northwestern.edu*
[b)]*s.webster@u.northwestern.edu*

Abstract. Laser metal additive manufacturing (AM) has become an increasingly popular technology due to its flexibility in geometry and materials. As one of the commercialized additive processes, powder-blown directed energy deposition (DED) has been used in multiple industries such as aerospace, automotive, medical device, etc. However, a lack of fundamental understanding remains for this process, and many opportunities for alloy development and implementation can be identified. A high-throughput, *in situ* DED system capable of multi-layer builds that can address these issues is presented here. Implications of layer heights and energy density are investigated through an extensive process parameter sweep, showcasing the power of a high-throughput setup while also discussing multi-layer interactions.

INTRODUCTION

Metal additive manufacturing (AM) has become an increasingly popular technology across multiple business sectors because of geometric complexity and material flexibility. Within this group of AM technologies, directed energy deposition (DED) is a broad family that includes wire-based and powder-based feeding mechanisms that can use electric arcs, electron beams, or lasers as heat sources (*1*). Laser, powder-blown DED has become a major focus within this group of technologies due to flexible processing (e.g., > 5-axis processing, not limited by wire geometry, and functionally graded material capability) (*2*). The process consists of a nozzle that uses carrier gas, such as argon, to blow powders onto a substrate where a laser (co-axial or off-angle from the powder flow) subsequently melts the deposited powders and substrate. The nozzle and laser can either move in tandem or the workpiece is translated below (in the most complex cases both movements occur at once) such that individual tracks and layers are created. Multiple layers of deposition and re-melting in this way leads to a fully realized metal part. DED has also become more popular because it offers a larger typical build capacity (2 m x 1.5 m x 0.75 m) and faster deposition speed (~70 cm^3/hour) compared to LPBF (0.5 m x 0.28 m x 0.325 m, 5-20 cm^3/hour) (*1*).

Despite the popularity of laser-based metal AM, fundamental knowledge gaps still exist. *In situ* studies utilizing synchrotron x-ray imaging (which has high temporal and spatial resolutions) for metal additive manufacturing have begun to address these gaps (*3*). Studies have investigated defect generation and elimination mechanisms, informed numerical models, and supported process monitoring systems. While most of the studies have focused on LPBF, powder-blown DED has started to be investigated in a similar vein.

Studies observing phenomena in LPBF have included understanding the formation of defects (such as porosity and hot cracking), the behavior of meltpool dynamics (spatter, internal flow), and laser-powder interactions (effective absorptivity) (*4–10*). Specifically, observance and analysis of the unstable vapor-liquid interface of the keyhole has been performed (*4, 6, 8, 11*). Measurements include the time of keyhole to collapse, frequency of oscillations, and evolution of the keyhole shape. The highest temporal resolution of keyhole measurement, thus far,

was achieved using ultrafast imaging at a frame rate of 10 MHz (*4*). Spatter ejection has also been characterized through qualitative observations and speed/angle of departure measurements (*4*, *7*, *12*). Pore formation has also been addressed in multi-layer LPBF scans, where three phenomena were observed: 1) liquid filling of previous layers' pores during remelting, 2) insufficient laser penetration to remelt/heal pores, and 3) merging of keyhole pores (*5*, *13*). Finally, internal flow behavior has been qualitatively and quantitatively measured using Tungsten (W) tracer particles (*14*, *15*). All these studies have led to a better understanding of metal powder AM processes; however, the rapid, stochastic addition of powders to the meltpool in DED will lead to different phenomena and behavior than what has been studied previously with highspeed *in situ* x-ray imaging in LPBF processes (*16–18*).

It is critical to understand the differences in defect formation, meltpool behavior, and laser-powder interactions for powder-blown processes in order to advance fundamental knowledge of the process, improve part quality, and support high-fidelity prediction models (*19*, *20*). The mechanism of powder particle addition to the meltpool in DED has started to be studied through macroscale highspeed imaging using commercial DED machines (*21*) and X-ray highspeed imaging using *in situ* set ups (*22–24*). Macroscale observations include powder particle melting and rebound behavior, while *in situ* studies have addressed the influence of process parameters on melt pool geometry and surface roughness (*24*, *25*). More recently, an *in situ* DED set up (BAMPR) utilized correlative X-ray imaging and *in situ* diffraction in order to acquire temperature history and measure in-plane stresses of multi-layer Inconel 718 builds to estimate its susceptibility to liquation cracking (*26*). The study also measured the melt pool's velocities using W tracer particles to understand the surface tension forces that govern melt pool shape. While these studies have revealed important mechanisms in multi-layer builds through *in situ* DED, the temporal and spatial resolutions are not high enough to capture individual particle-melt pool interactions.

Moreover, fast solidification rates and inherent temperature-dependent thermophysical properties lead to complex processing-structure relationships, complicating materials design for DED. Successful material systems and processing parameter maps have been difficult to create quickly. Currently, a new material system or processing window is developed through a large parameter sweep on a full-scale build and only gleans information (e.g., clad height and meltpool size) from the post-processing of samples (*27*). A smaller, faster system that can use lab-developed amounts of powder and give insight on *in situ* behavior is necessary to promote further materials development in DED. Additionally, a high-throughput system with these characteristics would support prediction models for material structure and performance through large data generation. It is important to consider the wide range of processing parameters in AM and the statistical information to support qualification for different materials. A high-throughput system would also enable the exploration of different processing regimes, such as the lack of fusion region which can be utilized in cementless implants (*28*), and the transitions between them.

Here we present the design of a high-throughput DED system with multi-layer capability and show data obtained from these types of experiments. A powder incorporation mechanism is identified, and the effect of energy density on multiple layers is discussed in the context of layer heights. Ti-6Al-4V is used in this study due to its popularity in lightweight applications, but any material system could be used with the designed machine. While similarities between the aforementioned BAMPR and the presented system exist (3-axis deposition stages, environmental chamber usage, multi-layer capability, powder flow rates on the order of ~0.2 g/min, and utilization of a ~200 µm laser spot size), the main differences between the systems are the process parameter capabilities and use of a high-throughput stage/fixture. The high-throughput system utilizes a deposition speed of 50-500 mm/s to accommodate faster image acquisition and sample processing rates while the BAMPR utilizes 1-5 mm/s for industrial replication. The maximum laser power achieved by the high-throughput system is 500 W, while the BAMPR has a maximum of 200 W. Finally, powder delivery methods are different where the high-throughput system uses an angled powder nozzle and the BAMPR uses a coaxial nozzle. It is noted here that without information on the spatial distribution of the powder flow in the BAMPR nozzle, a complete comparison with the presented system cannot be made. In all, the presented high-throughput system can process samples at a faster rate and is better equipped for fundamental powder incorporation studies while maintaining a sufficient energy density for deposition.

METHODS AND MATERIALS

In Situ Experimental Setup

Highspeed, phase-contrast imaging at the Advanced Photon Source (APS) was used to observe *in situ* phenomena using a high-throughput DED system. Experiments were conducted at beamline 32-ID-B using an intense white x-ray beam from a short period undulator (U18) source, with a main energy of 24 keV. The experimental principle is

shown in schematic form in Fig. 1. A custom nozzle is used to deposit Ti-6Al-4V powders onto a small, rectangular Ti-6Al-4V substrate, where both are concurrently melted with a laser to fabricate a single DED clad. Each clad is imaged perpendicularly to the processing and deposition direction using the x-ray beam, as shown in Fig. 1. The procedure during an experiment was the following: powder hopper is turned on, powder stabilizes for 10 s, x-ray shutter opens, laser and deposition set ups are triggered, single powder layer is melted onto the substrate, x-ray beam image is converted to visual image through a scintillator and captured by the highspeed camera. The duration of a typical experiment is 31 ms and varies with the laser scan speed. To reiterate, *in situ* images are taken from the front face of the substrate using the x-ray beam during deposition; images in this study were taken at 30,000 fps with an exposure time of 12 μs. This frame rate and exposure time were chosen such that particles created linear streaks that could be used for velocity measurements. The field of view in this study is 2 mm by 2 mm.

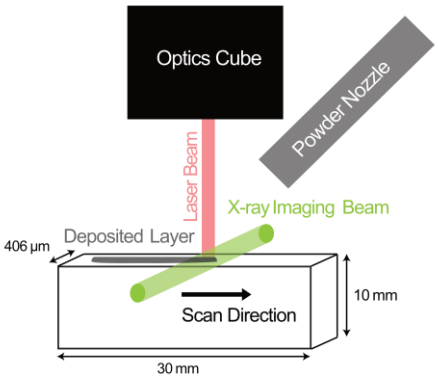

FIGURE 1. Orientation of Ti-6Al-4V sample with deposition direction and x-ray imaging beam. The sample is imaged from the front-facing plane of the substrate (30 mm x 10mm) and the direction of deposition is from left to right across the top-facing plane of the substrate (30 mm x 406 **μ**m and 812 **μ**m).

The size limitations of the x-ray experimental hutch required a small-scale DED system in order to perform *in situ* experiments, Fig. 2. The full system consists of the following components: deposition set-up, 500 W Ytterbium fiber laser (1,070 nm), multi-material commercial GTV powder hopper, scintillator, and highspeed camera. The fiber laser is used to melt the powders and substrate during processing, and the x-ray beam is used for phase-contrast imaging. The GTV powder hopper can hold up to two types of material and can achieve mass flowrates from 99 mg/s to 745 mg/s (volumetric flowrates from 79.2 cm^3/hr to 604 cm^3/hr), similar to that of a commercial DED system. The environmental chamber houses the deposition setup and is filled with argon and maintained at an oxygen level of <1.0% using an LC technology oxygen analyzer and controller. The oxygen content of the environmental chamber is higher in this study than in typical commercial systems because the goal was to prevent spontaneous combustion and minimize oxidation, which sacrifices some resulting material quality. The deposition setup uses a linear stage that moves from left-to-right; this stage contains the mounted laser optics, in-house powder nozzle, sample alignment camera, and powder alignment stage.

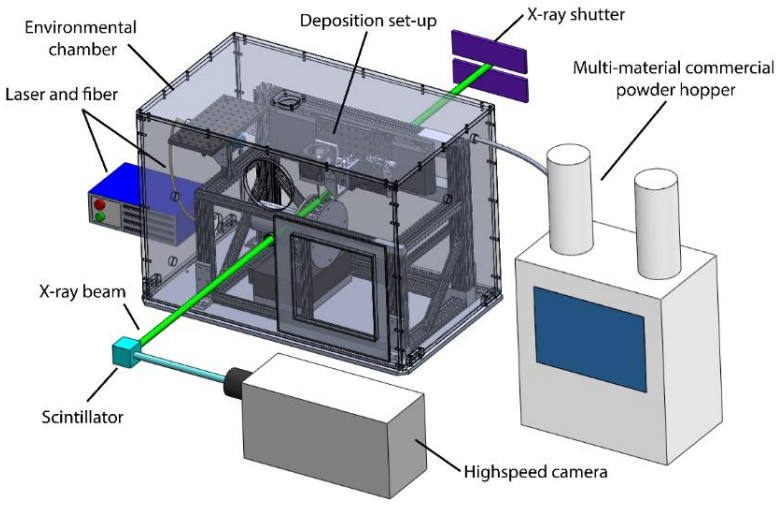

FIGURE 2. X-ray hutch setup consisting of an environmental chamber, linear deposition system, multi-material powder hopper, Ytterbium laser, scintillator, and highspeed camera.

Deposition Set-up

A 50 mm optics cube holds a dichroic mirror and 100 mm planoconvex focusing lens. The main processing beam (1,070 nm, TEM_{00}, IPG YLR-500-AC, IPG Photonics, USA) is reflected by the dichroic mirror towards the substrate, while the red laser guide light (600-700 nm) is transmitted for alignment purposes, Fig. 3 (a). The focusing lens provides a 235 μm spot size for the main processing laser which is defocused ~2 mm below the focus plane of the lens in order to maintain a proper energy density for the substrate size and material. In order to ensure repeatability, three alignments must be maintained in the deposition set up: 1) the center of the powder nozzle is aligned with centerline of the top face of the substrate, 2) the laser must be in-line with the centerline of the top face of the substrate, 3) the powder focal point is incident with the laser. Each alignment is maintained through the following methods: 1) a manual three-axis stage aligns the powder nozzle with the centerline of the substrate, 2) a CCD camera visualizes the top face of the substrate where the red laser guide light aligns the laser with the substrate centerline, and 3) a custom fixture holds the powder nozzle at a distance of 5 mm away from the substrate at a 46° angle where the powder focal point occurs.

The powder nozzle used in this study was designed and built in-house; it is a converging-diverging nozzle with a 1 mm exit that has a 1.5 mm powder spread at the deposition surface, Fig. 3 (b). Since the substrate thickness ranges between 406 μm and 812 μm, the powder spread was minimized as much as possible. Additionally, minimal divergence of the powder stream occurs after exiting the nozzle, providing a robust powder focus that will not change even if the distance between the substrate and powder nozzle changes by ±1 mm. The nozzle design is also modular, enabling future studies on effects of powder distributions.

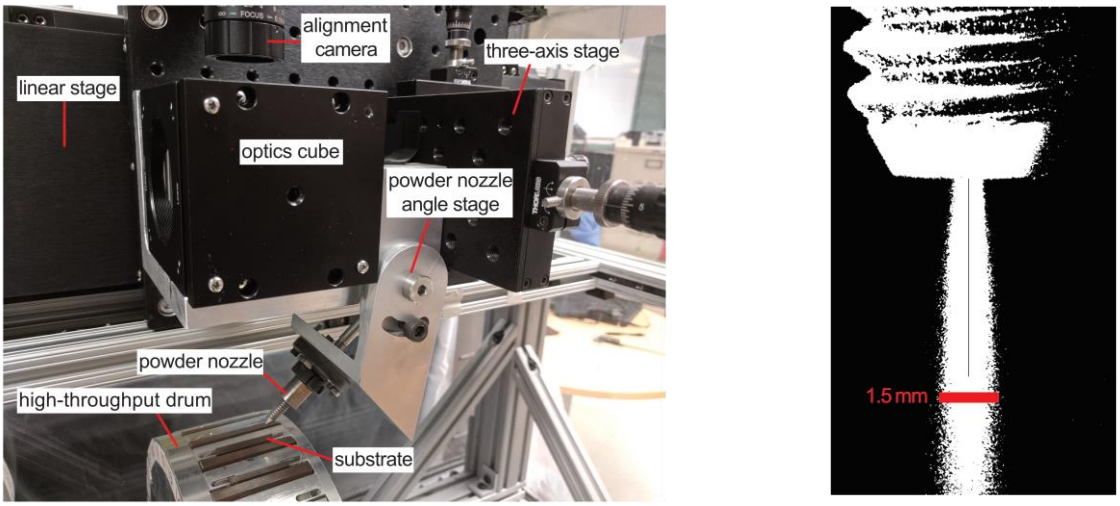

(a) (b)

FIGURE 3. (a) Deposition system that contains the laser optics and powder nozzle for DED. (b) Modular powder nozzle with a spread of 1.5 mm.

High-throughput Drum Design

The high-throughput drum minimizes the time between sample runs and system purges, thus maximizing the number of explored parameters and the number of sample repetitions that can be achieved in a given amount of time. Multiple time-saving factors were considered when designing the high-throughput drum, shown in Fig. 4 for the *in situ* DED system. These factors include: a space-efficient sample drum, magnet actuated sample holders for fast loading and unloading, the use of two interchangeable drums, and an automated controller for environmental chamber re-use.

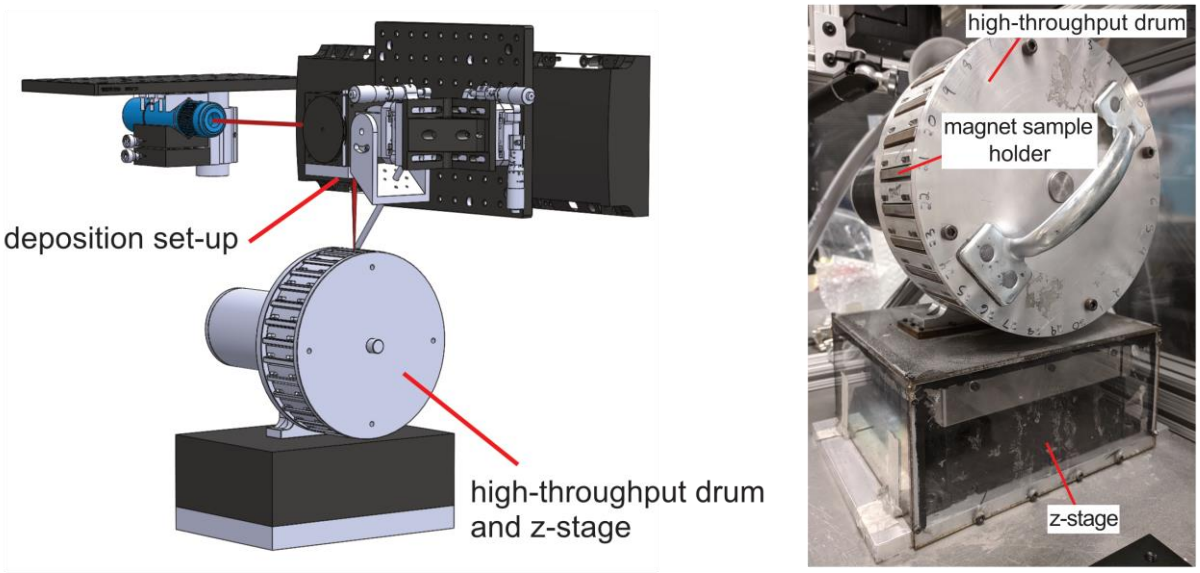

FIGURE 4. High-throughput sample drum that enables multi-layer deposition and exploration of large parameter space. Samples are held in place with strong magnets. Up to 30 samples can be held at one time.

Each drum holds a maximum of 30 samples, where the limiting factor was the height between the bottom of the environmental chamber and the focal plane of the processing laser. Each sample is held in place by rectangular magnets for simple, fast loading and unloading, shown in Fig. 4. Due to the size limitations of the x-ray hutch and environmental chamber, the designed sample holder needed to be space-efficient while holding as many samples as possible. A rotating drum containing slots for each sample is used to reduce the amount of space used by the stage and holder to switch from one sample to another (compared to the displacement needed by a linear stage and sample holder. Additionally, two drums were manufactured so that substrates could be replaced during current experiments in preparation for the next run of a drum.

Perhaps the most critical factor in this design is utilizing an automated controller for the drum rotation and deposition stage, where time can be saved through continuous use of the environmental chamber. An inert environment must be maintained throughout the build process to minimize oxidation and prevent any combustion of reactive materials. Although a single experiment only takes approximately 31 ms with this deposition system, purging the environmental chamber of oxygen after each sample would require about 15 minutes. Processing 30 samples, in that case, would take approximately 7.5 hours, not including sample exchange time and would also use ten times as much argon. In this study, 30 samples were processed in approximately 1.5 hours, a 5-fold reduction in processing time.

Finally, the drum and rotational stepping motor sit on a z-stage that can be raised and lowered, enabling multi-layer deposition. A multi-layer build is created through a series of single layer depositions as described in Section 2.1. The sample is moved down between each single layer scan, where the top of the previously deposited clad is moved to the focal plane of the laser. This height changes for different processing parameters but ensures the same laser spot size of 235 μm for each layer. Additionally, the rotational accuracy of the stepping motor that drives the drum is fractions of a degree, such that the top surface of each substrate is as perpendicular as possible to the processing laser during deposition in order to maintain a repeatable, uniform spot size. Each multi-layer sample consists of four layers with the scan direction always set from left to right. Layer interaction phenomena and powder deposition dynamics can thus be more fully understood using this setup.

Substrate and Powder Materials

The substrate and powder materials in this study are grade 5 titanium alloy Ti-6Al-4V. Wire EDM was used to cut rectangular substrates dimensioned 30 mm by 10 mm from 406 μm and 812 μm thick, 12” x 12” sheets. The powders are AP&C Spherical APA Ti-6Al-4V, 45 μm-106 μm in diameter with a Gaussian size distribution. Industrial grade argon is used as shield gas in the powder nozzle and purge gas in the environmental chamber.

Laser Beam Diameter Measurement

The laser spot size at the substrate surface for this study was approximated at 235 μm, which was measured from the keyhole width. FIJI was used for image processing and keyhole width measurements (*29*); the keyhole width measurement was taken at the top of the keyhole/substrate and an average was calculated using two experimental runs on a blank substrate with no powder. It is noted that the Gaussian beam profile cannot be fully captured by this measurement due to attenuation at the outside of the laser spot; however, to minimize these effects, the highest laser power available was used during a bare plate scan. It is estimated that the lowest 15% of the beam is perhaps not captured, which means the actual beam dimeter could be ~35 μm larger than the reported value.

Experimental Procedures

The high-throughput drum enables the exploration of a large parameter space. In this study, experiments were performed at a scan speed of 100 mm/s while laser power and scan speed were varied from 208 W- 506 W and 196 mg/s – 400 mg/s, respectively. Each range was chosen based on initial testing of the ‘parameter window’ (i.e., a solid clad is created and a keyhole does not occur) for Ti-6Al-4V with this setup. The specific combinations of parameters used in this study is shown in Table 1. Each set of parameters was performed three times as a single line scan with one repetition as a multi-layer build with four layers to observe multi-layer phenomena.

TABLE 1. Processing parameters for given S' values.

$S' = \frac{J/kg}{mm^2/s}$	Laser Power (W)	Powder Flowrate (mg/s)
28	208	400
	231	435
30	225	400
	231	410
34	254	400
	231	370
40	294	400
	231	322
46	345	400
	231	279
56	414	400
	231	236
68	506	400
	231	196

The choice of process parameters in this study is based on the ratio of mass and energy input per unit area and time of DED processing, or specific energy density S. It is defined as the following:

$$S' = \frac{P}{\dot{m} \cdot A_{beam} \cdot \tau} = \left[\frac{J/g}{mm^2/s}\right], \; where \; \tau = v/d_{beam} \tag{1}$$

where P is laser power, $\dot{m}$ is powder mass flowrate, v is scan speed, and d_{beam} is the diameter of the laser beam. Laser power and powder mass flowrate levels were chosen in order to create 7 pairs of unique S values for comparison of build conditions (i.e., clad height) within the specified ranges above.

Image Processing Method

The image taken at t_0 is subtracted from t_1, where the resulting image is the difference in intensities at each pixel between the two time steps. The intensity difference can be very small, so the resulting difference image is normalized based on its maximum intensity to enhance contrast. After this normalization, the differential image shows what has moved between the two frames t_0 and t_1, Fig. 5. The full imaging process technique is shown mathematically as:

$$I_{t_n} - I_{t_{n-1}} = I_n^{diff} \rightarrow \frac{I_n^{diff}}{\max\left(I_n^{diff}\right)} = I_n^{norm} \tag{2}$$

where I_{t_n} is the intensity of the image at time t_n, $I_{t_{n-1}}$ is the intensity of the image in the previous frame at time t_{n-1}, I_{diff} is the resulting intensity after subtraction, and I_{norm} is the normalized subtracted image. This operation is performed for each timestep in the experimental sequence, where *n* ranges from 1 to the total number of timesteps or frames captured in the experiment.

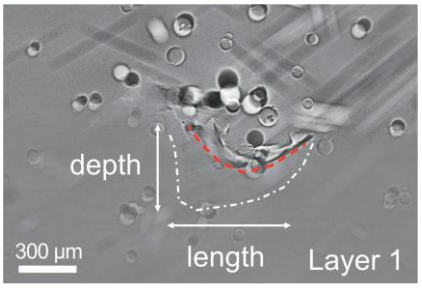

FIGURE 5. (a) Subtracted image of frames 0.033 ms apart in the first layer of deposition. The meltpool is outlined by a white dash-dot line and the vapor depression is outlined by a red dashed line. The measured meltpool depth and length are indicated.

RESULTS AND DISCUSSION

The raw data collected using this high-throughput, *in situ* setup consists of many grayscale images. It is a very rich data set due to the high spatiotemporal resolution. Multiple phenomena in powder-blown DED can be observed including: melt pool geometry, spattering, powder incorporation, and layer interactions. Results presented here include effect of laser power and powder flowrate on layer heights, surface roughness as a function of layer number, and observations of multi-layer interactions. A total of 178 samples were built in this study to explore a wide variety of parameters; this showcases the efficiency of using a high-throughput system. A subset of 89 samples was analyzed for the results presented here. A representative image of the raw data obtained for multi-layer depositions is shown in Fig. 6, where each of the four layers is shown during deposition; the result of deposition is a four-layer thin wall. Images were collected at 30,000 fps for each layer.

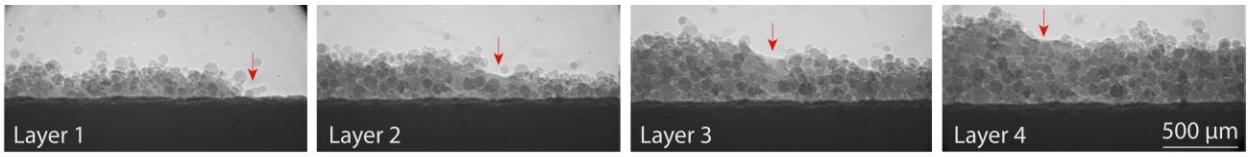

FIGURE 6. Example of a multi-layer build, showing each layer in the process of deposition. Red arrows indicate the position of the laser in the image (laser power 208 W and mass flowrate 400 mg/s).

The average layer height for each sample was determined by thresholding the grayscale image for the newly deposited powder layer and averaging the height of the pixel columns contained within that layer. X-ray computed tomography (CT) was performed on representative samples to verify that the layer heights in the X-ray images match the actual height of the sample; it was found that powders fully melted in all conditions and that any surface roughness is attributed to powders partially melting and attaching to the outer clad surface, as occurs in industrial DED. The layer heights range from 100 µm to 400 µm, and the layer height increases with increasing laser power and powder flowrate, Fig. 7, which is expected from macroscale experimental literature (*30*).

(a)

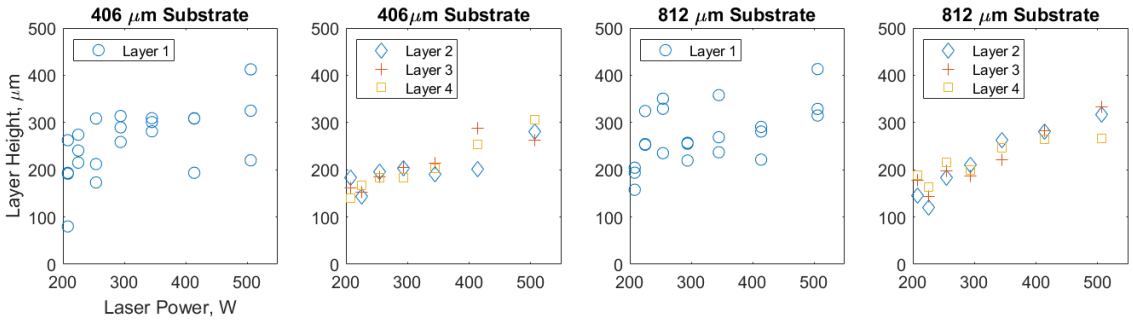

(b)

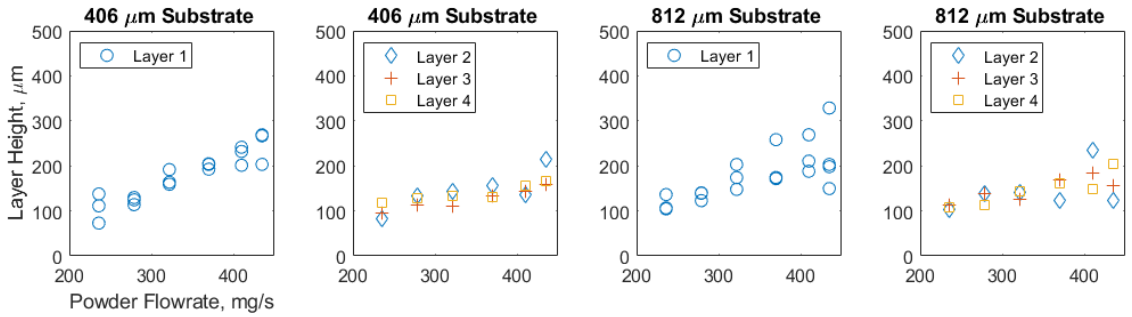

FIGURE 7. (a) Layer height as a function of laser power for different substrate thicknesses and layer numbers, powder flowrate was kept constant at 400 mg/s. (b) Layer height as a function of powder flowrate for different substrate thicknesses and layer numbers, laser power was kept constant at 231 W. On average, the first layer of deposition was larger than layers 2-4. Both an increase in laser power and powder flow rate led to taller layer heights, as expected.

There is no significant influence of substrate thickness on the layer height, despite over-melting in the thinner substrates (where powders adhered to the side of the substrate as it melted over). The first layer of deposition had more variation than layers 2-4 and was taller on average than subsequent layers. A one-way Anova analysis was performed in Matlab to determine if the first layer was significantly taller than layers 2-4, Figure 8 (a). It is clear through the multiple comparison test, Fig. 8 (b), that the mean height of layer 1 is about 55 μm larger than layers 2-4 with a 95% confidence interval.

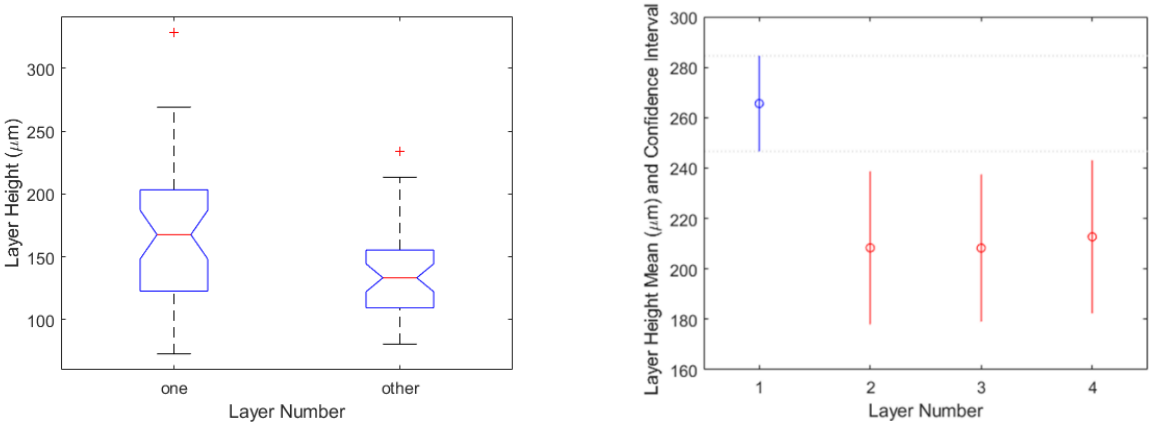

(a) (b)

FIGURE 8. (a) One-way Anova results showing distribution of layer heights for the first layer and all other layers. (b) Mean layer height and 95% confidence interval for each layer number. The first layer had a taller layer height on average.

In general, it was observed that the second layer of the multi-layer builds has a more uniform height across the substrate. The first layer typically had large 'hills' of powder which would be filled in through layers 2-4, which is represented in the larger variation in the mean height. The 'layer correction' between the first layer and second layer is shown in Fig. 9 (a), where the second layer has fewer crevices and hills of powder than the first layer. Figure 9 (b) shows a series of images depicting the largest 'hill' of powder being melted into the second layer. When the laser becomes incident on the tallest powders, they quickly melt and fall towards the meltpool. Once melted they are joined with any incoming particles or re-melted powders from the previous layers.

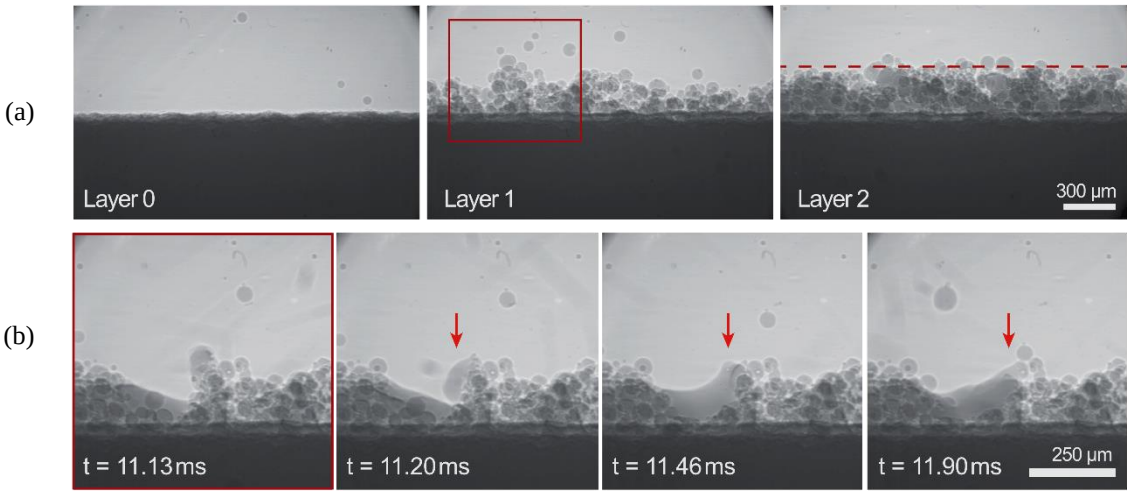

FIGURE 9. (a) Substrate surface, first layer deposition, and second layer deposition (laser power 231 W and powder mass flowrate 279 mg/s). Uniformity of surface height is improved on the second layer, however, melting of large 'hills' of powder affect the meltpool surface. (b) Second layer powder incorporation mechanism, where tall powders are melted and incorporated into the meltpool.

This layer correction is also quantified by the average and standard deviation of R_a for each layer number, shown in Table 2. The first layer of deposition had an average R_a of 110.8 (µm) while the average R_a of layers 2, 3, and 4 were approximately 90 (µm). This multi-layer observation is important because it differs from powder incorporation mechanisms within the first layer deposition on the substrate. In the first layer, powders will either 'stick' to the meltpool or enter the meltpool as a solid and subsequently melt (*18*). In the second layer, both of these mechanisms can occur in addition to powder incorporation via 'layer correction' where tall clumps of partially melted powders are fully melted and incorporated into the meltpool. This will influence meltpool dynamics by changing the stability of the front edge of the meltpool. In the third image of Fig. 9 (b), it is shown that the meltpool reaches up to the melted powders and will invariably rescind back due to gravity. Repetitions of these mechanisms could lead to a more violent meltpool surface in the second layer than the first layer. Further analysis of this observed mechanism is required in order to fully understand the evolution of the meltpool surface and further determine how layers interact with one another. It is evident that the high-throughput nature of the setup enables calculation of statistical information and repeatability while also capturing highly detailed phenomena.

TABLE 2. Surface roughness (R_a) of each layer number.

Layer Number	Average R_a (µm)	Standard Deviation R_a (µm)
1	110.8	44.9
2	88.4	34.2
3	89.8	32.5
4	91.9	28.7

Observations were also be made by looking at the difference of two timeframes, rather than the raw images, to observe the meltpool. The difference is obtained by subtracting the current time step from the previous time step (4). In this way, any object that has moved between the frames can be visualized. Figure 10 (a) shows the representative image of the meltpool on the first deposited layer, where it is clearly visible within the substrate. The fourth layer does not have the same deep meltpool; instead, a shallow meltpool remains very near the vapor depression outline, Fig. 10 (b). This is a clear depiction of the difference in meltpool conditions for deposition on the substrate versus deposition on a previously melted powder layer, where the surface roughness of un-melted powders leads to higher scattering of the laser beam and decreases absorption of the sample. This is not reflected in macroscale builds because heat is not accumulated in the substrate as more layers are built, but it is expected at this small scale. The

change in absorptivity (and melt pool depth) is also reflected in the reported mean layer heights, where the first deposited layer is taller.

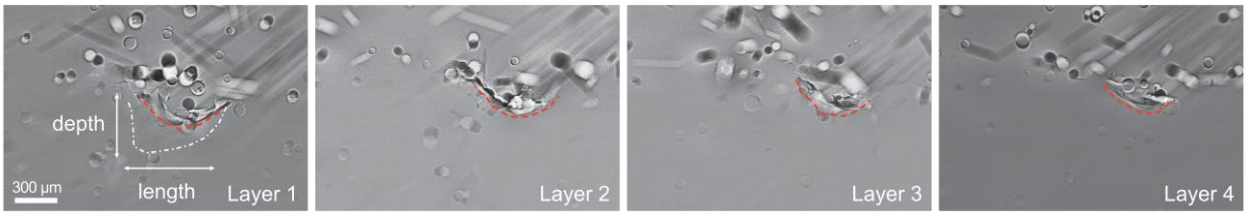

FIGURE 10. Subtracted image of frames 0.033 ms apart in each layer of deposition. The meltpool is outlined by a white dash-dot line and the vapor depression is outlined by a red dashed line. The measured meltpool depth and length is indicated in white. This experiment used a laser power of 414 W and powder mass flowrate of 400 mg/s.

Implications of layer heights in a multi-layer build are also shown through this study. Energy density is typically used to define the build conditions in DED and connected with layer heights, however, multi-layer builds in this study show that a disparity in energy density occurs even when the ratio of laser power to mass flowrate is maintained. Figure 11 (a) shows an experiment with a laser power of 345 W and a powder mass flowrate of 400 mg/s, while Fig. 11 (b) shows an experiment with a laser power of 231 W and a powder mass flowrate of 279 mg/s. Both experiments have an S' level of 45 $\frac{\mathbf{J/kg}}{\mathbf{mm^2/s}}$ but the average height of the clads are (a) 427 µm and (b) 678 µm, respectively. It is important to note this discrepancy because a difference of approximately 250 µm in every four layers can lead to build failure due to the change in powder and laser beam focus (*31*); therefore, global energy density is not a good parameter to use for clad height prediction. In all, further studies using this setup can be used to develop an appropriate relationship of processing parameters to meltpool size and clad height for a given material system. Meltpool measurements can additionally be used to validate high fidelity CFD models of DED.

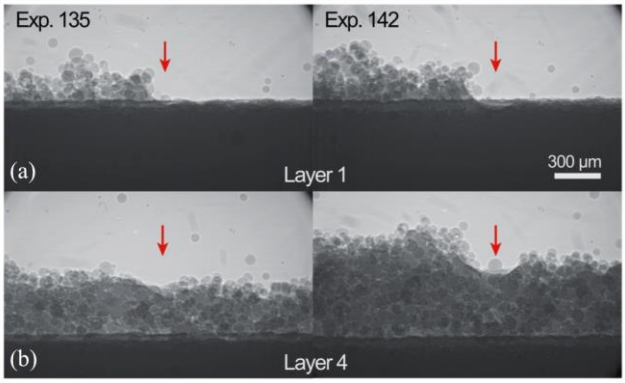

FIGURE 11. (a) First and fourth layer deposition of an experiment with a laser power of 345 W and a powder mass flowrate of 400 mg/s. (b) First and fourth layer deposition of an experiment with a laser power of 231 W and a powder mass flowrate of 279 mg/s. Red arrows indicate position of the laser during build. Height of clad in (b) is approximately 250 µm taller than that of (a) but both experiments have the same $\boldsymbol{S'}$ ratio.

CONCLUSION

The *in situ* DED system designed in this study is aimed at the development of fundamental knowledge of multi-layer DED manufacturing processes. Highspeed phenomena such as powder-meltpool and layer interactions can be observed while maintaining a high-throughput workspace. The use of the high-throughput system decreased the amount of processing time by a factor of 5 times compared to typical *in situ* x-ray imaging procedures. A comparison of mean layer heights showcased the power of a high-throughput setup, where the first layer was 55 µm taller than subsequent layers, while high spatiotemporal images were used to identify changes in melt pool depth.

Additionally, a potential powder incorporation mechanism was identified, where differences in height within the first layer are 'smoothed out' after re-melting in the second layer. Finally, the implications of layer height and global energy density were discussed for multi-layer builds. This study ultimately shows that this setup enables exploration of large parameter sets and could be used to quickly develop processing windows for new material systems in DED while maintaining high spatiotemporal resolution of *in situ* DED experiments.

ACKNOWLEDGMENTS

The authors would like to acknowledge Niranjan Parab and Sarah Wolff for their support at APS, as well as Marisa Bisram, Zoe Granato, and Shuheng Liao for experiment execution. This research used resources of the Advanced Photon Source, a U.S. Department of Energy (DOE) Office of Science User Facility operated for the DOE Office of Science by Argonne National Laboratory under Contract No. DE-AC02-06CH11357. This research was also funded by NIMSI and NIST CHiMaD under grant No.70NANB14H012

AVAILABILITY OF DATA

The data that support the findings of this study are available from the corresponding author upon reasonable request.

REFERENCES

1. T. Debroy, H. L. Wei, J. S. Zuback, T. Mukherjee, J. W. Elmer, J. O. Milewski, A. M. Beese, A. Wilson-heid, A. De, W. Zhang, Progress in Materials Science Additive manufacturing of metallic components – Process , structure and properties. *Prog. Mater. Sci.* **92**, 112–224 (2018).
2. S. Alya, R. Singh, Discrete Phase Modeling of the Powder Flow Dynamics and the Catchment Efficiency in Laser Directed Energy Deposition with Inclined Coaxial Nozzles. *J. Manuf. Sci. Eng. Trans. ASME*. **143** (2021), doi:10.1115/1.4049966.
3. T. Sun, W. Tan, L. Chen, A. Rollett, In situ/operando synchrotron x-ray studies of metal additive manufacturing. *MRS Bull.* **45**, 927–933 (2020).
4. N. D. Parab, C. Zhao, R. Cunningham, L. I. Escano, K. Fezzaa, W. Everhart, A. D. Rollett, L. Chen, T. Sun, Ultrafast X-ray imaging of laser–metal additive manufacturing processes. *J. Synchrotron Radiat.* **25**, 1467–1477 (2018).
5. L. Sinclair, C. L. A. Leung, S. Marussi, S. J. Clark, Y. Chen, M. P. Olbinado, A. Rack, J. Gardy, G. J. Baxter, P. D. Lee, In situ radiographic and ex situ tomographic analysis of pore interactions during multilayer builds in laser powder bed fusion. *Addit. Manuf.* **36**, 101512 (2020).
6. A. A. Martin, N. P. Calta, J. A. Hammons, S. A. Khairallah, M. H. Nielsen, R. M. Shuttlesworth, N. Sinclair, M. J. Matthews, J. R. Jeffries, T. M. Willey, J. R. I. Lee, Ultrafast dynamics of laser-metal interactions in additive manufacturing alloys captured by in situ X-ray imaging. *Mater. Today Adv.* **1**, 100002 (2019).
7. C. Zhao, K. Fezzaa, R. W. Cunningham, H. Wen, F. De Carlo, L. Chen, A. D. Rollett, T. Sun, Real-time monitoring of laser powder bed fusion process using high-speed X-ray imaging and diffraction. *Sci. Rep.* **7**, 1–11 (2017).
8. R. Cunningham, C. Zhao, N. Parab, C. Kantzos, J. Pauza, K. Fezzaa, T. Sun, A. D. Rollett, Keyhole threshold and morphology in laser melting revealed by ultrahigh-speed x-ray imaging. *Science (80-.).* **363**, 849–852 (2019).
9. Q. Guo, C. Zhao, M. Qu, L. Xiong, L. I. Escano, S. M. H. Hojjatzadeh, N. D. Parab, K. Fezzaa, W. Everhart, T. Sun, L. Chen, In-situ characterization and quantification of melt pool variation under constant input energy density in laser powder bed fusion additive manufacturing process. *Addit. Manuf.* **28**, 600–609 (2019).
10. B. J. Simonds, J. R. Tanner, A. Artusio-Glimpse, P. A. Williams, N. D. Parab, C. Zhao, T. Sun, The Causal Relationship between Melt Pool Geometry and Energy Absorption Measured in Real Times During Laser-Based Manufacturing. *Submitted*. **23**, 101049 (2021).
11. C. Zhao, N. D. Parab, X. Li, K. Fezzaa, W. Tan, A. D. Rollett, T. Sun, Critical instability at moving keyhole tip generates porosity in laser melting. *Science (80-.).* **370**, 1080–1086 (2020).
12. C. L. A. Leung, S. Marussi, R. C. Atwood, M. Towrie, P. J. Withers, P. D. Lee, In situ X-ray imaging of defect and molten pool dynamics in laser additive manufacturing. *Nat. Commun.* **9**, 1–9 (2018).

13. Y. Chen, S. J. Clark, C. L. A. Leung, L. Sinclair, S. Marussi, M. P. Olbinado, E. Boller, A. Rack, I. Todd, P. D. Lee, In-situ Synchrotron imaging of keyhole mode multi-layer laser powder bed fusion additive manufacturing. *Appl. Mater. Today*. **20**, 100650 (2020).
14. L. Aucott, H. Dong, W. Mirihanage, R. Atwood, A. Kidess, S. Gao, S. Wen, J. Marsden, S. Feng, M. Tong, T. Connolley, M. Drakopoulos, C. R. Kleijn, I. M. Richardson, D. J. Browne, R. H. Mathiesen, H. V. Atkinson, Revealing internal flow behaviour in arc welding and additive manufacturing of metals. *Nat. Commun.* (2018), doi:10.1038/s41467-018-07900-9.
15. Q. Guo, C. Zhao, M. Qu, L. Xiong, S. M. H. Hojjatzadeh, L. I. Escano, N. D. Parab, K. Fezzaa, T. Sun, L. Chen, In-situ full-field mapping of melt flow dynamics in laser metal additive manufacturing. *Addit. Manuf.* **31**, 100939 (2019).
16. A. Aggarwal, A. Chouhan, S. Patel, D. K. Yadav, A. Kumar, A. R. Vinod, K. G. Prashanth, N. P. Gurao, Role of impinging powder particles on melt pool hydrodynamics, thermal behaviour and microstructure in laser-assisted DED process: A particle-scale DEM – CFD – CA approach. *Int. J. Heat Mass Transf.* **158**, 119989 (2020).
17. A. Chouhan, A. Aggarwal, A. Kumar, A computational study of porosity formation mechanism, flow characteristics and solidification microstructure in the L-DED process. *Appl. Phys. A Mater. Sci. Process.* **126**, 1–12 (2020).
18. J. C. Haley, J. M. Schoenung, E. J. Lavernia, Modelling particle impact on the melt pool and wettability effects in laser directed energy deposition additive manufacturing. *Mater. Sci. Eng. A*. **761**, 138052 (2019).
19. W. Yan, S. Lin, O. L. Kafka, C. Yu, Z. Liu, Y. Lian, S. Wolff, J. Cao, G. J. Wagner, W. K. Liu, Modeling process-structure-property relationships for additive manufacturing. *Front. Mech. Eng.* **13**, 482–492 (2018).
20. H. Tian, X. Chen, Z. Yan, X. Zhi, Q. Yang, Z. Yuan, Finite-element simulation of melt pool geometry and dilution ratio during laser cladding. *Appl. Phys. A*. **125**, 485 (2019).
21. J. C. Haley, J. M. Schoenung, E. J. Lavernia, Observations of particle-melt pool impact events in directed energy deposition. *Addit. Manuf.* **22**, 368–374 (2018).
22. S. Wolff, H. Wu, N. D. Parab, C. Zhao, K. Ehmann, T. Sun, J. Cao, In-situ high-speed X-ray imaging of piezo-driven directed energy deposition additive manufacturing. *Sci. Rep.* (2019), doi:10.1038/s41598-018-36678-5.
23. S. Webster, S. J. Wolff, N. D. Parab, B. Aronson, B. Gould, A. Greco, T. Sun, In-situ Observations of Directed Energy Deposition Additive Manufacturing Using High-Speed X-ray Imaging. *JOM* (2020), doi:10.1007/s11837-020-04469-x.
24. Y. Chen, S. Clark, A. C. L. Leung, L. Sinclair, S. Marussi, R. Atwood, T. Connoley, M. Jones, G. Baxter, P. D. Lee, Melt pool morphology in directed energy deposition additive manufacturing process. *IOP Conf. Ser. Mater. Sci. Eng.* **861** (2020), doi:10.1088/1757-899X/861/1/012012.
25. Y. Chen, S. J. Clark, Y. Huang, L. Sinclair, C. Lun Alex Leung, S. Marussi, T. Connolley, O. V. Magdysyuk, R. C. Atwood, G. J. Baxter, M. A. Jones, I. Todd, P. D. Lee, In situ X-ray quantification of melt pool behaviour during directed energy deposition additive manufacturing of stainless steel. *Mater. Lett.* **286**, 129205 (2021).
26. Y. Chen, S. J. Clark, D. M. Collins, S. Marussi, S. A. Hunt, D. M. Fenech, T. Connolley, R. C. Atwood, O. V. Magdysyuk, G. J. Baxter, M. A. Jones, C. L. A. Leung, P. D. Lee, Correlative Synchrotron X-ray Imaging and Diffraction of Directed Energy Deposition Additive Manufacturing. *Acta Mater.* **209**, 116777 (2021).
27. N. A. Kistler, A. R. Nassar, E. W. Reutzel, D. J. Corbin, A. M. Beese, Effect of directed energy deposition processing parameters on laser deposited Inconel ® 718: Microstructure, fusion zone morphology, and hardness. *J. Laser Appl.* **29**, 022005 (2017).
28. T. Y. Kwak, J. Y. Yang, Y. B. Heo, S. J. Kim, S. Y. Kwon, W. J. Kim, D. H. Lim, Additive manufacturing of a porous titanium layer structure Ti on a Co–Cr alloy for manufacturing cementless implants. *J. Mater. Res. Technol.* **10**, 250–267 (2021).
29. J. Schindelin, I. Arganda-Carreras, E. Frise, V. Kaynig, M. Longair, T. Pietzsch, S. Preibisch, C. Rueden, S. Saalfeld, B. Schmid, J. Y. Tinevez, D. J. White, V. Hartenstein, K. Eliceiri, P. Tomancak, A. Cardona, Fiji: An open-source platform for biological-image analysis. *Nat. Methods*. **9**, 676–682 (2012).
30. B. Bax, R. Rajput, R. Kellet, M. Reisacher, Systematic evaluation of process parameter maps for laser cladding and directed energy deposition. *Addit. Manuf.* **21**, 487–494 (2018).
31. D. S. Shim, G. Y. Baek, J. S. Seo, G. Y. Shin, K. P. Kim, K. Y. Lee, Effect of layer thickness setting on deposition characteristics in direct energy deposition (DED) process. *Opt. Laser Technol.* **86**, 69–78 (2016).